Available online at www.sciencedirect.com
SCIENCE DIRECT®
Electrochimica Acta 50 (2005) 1405–1412
ELECTROCHIMICA Acta
www.elsevier.com/locate/electacta

Electrodeposition of amorphous/nanocrystalline and polycrystalline Ni–Mo alloys from pyrophosphate baths

Mikołaj Donten[a], Henrikas Cesiulis[b], Zbigniew Stojek[a,*,1]

[a] *Department of Chemistry, Warsaw University, ul. Pasteura 1, PL-02-093 Warsaw, Poland*
[b] *Department of Physical Chemistry, Vilnius University, Naugarduko 24, LT-2006, Vilnius, Lithuania*

Received 20 July 2004; received in revised form 16 August 2004; accepted 21 August 2004
Available online 3 October 2004

Abstract

Pyrophosphate plating bath was found to be a good alternative to citrate bath for deposition of Ni–Mo amorphous alloys. The addition of wetting agents such as 2-butyne-1,4-diol and rokafenol N-10 to the pyrophosphate bath resulted in the removal of bumps, spheres and cracks from the Ni–Mo alloy surface. The plated alloy layers adhered well to Cu–Zn brass and steel, were of thickness from a fraction to tens of micrometers and the molybdenum content was independent of the distance from the support. An increase in the concentration of the molybdate ion in the bath leads to an increase in the amount of Mo in the alloys up to 33–35 at.% and to a decrease in the deposition rate. These changes and the influence of pH are discussed in the paper. The atom arrangement in the alloys changes from (2 2 0) preferred for pure-nickel deposition to (1 1 1) for content of Mo higher than 15 at.%. For 20 and more at.% of Mo the structure of the alloy is amorphous like. An analysis of SEM and STM micrographs obtained indicates that contrary to the Ni–W alloy the "amorphous" phase is made of circa 10–50 nm in diameter objects and not by long needles perpendicular to the substrate.

Keywords: Electrodeposition; Ni–W alloys; Amorphous alloys; Pyrophosphate bath

1. Introduction

Nickel–molybdenum alloys are of interest due to their useful properties. They are resistant to corrosion (also in the corrosion media containing Cl^- ions) and wear, exhibit low thermal-expansion coefficients, are known of premium hardness and premium catalytic properties, and some of them have unusually soft magnetic characteristics [1–7]. Regarding the resistance to corrosion, the alloy films probably cannot be too thin to be effectively resistant. The large catalytic activity of Ni–Mo alloys comes not only from the significant content of nickel, a main component, but also from the unique amorphous internal structure of the alloy. The presence of molybdenum in these materials apparently increases their catalytic activity and improves their mechanical properties. The high electrochemical activity and relatively low cost of the Ni–Mo alloys make them widely used in modern electrochemistry-related industry [3–5]. Applications of the Ni–W alloys include their use as electrodes to promote the hydrogen evolution [3–5] and as catalysts in the hydro processing of aromatic oils [6] and hydrogenation of benzene in the gas phase [7].

Ni–Mo alloys can be prepared using several methods. Metallurgical methods are not very convenient because of easy oxidation at the crystallisation step and high melting temperature of molybdenum. To prepare the molybdenum alloys, other advanced processing methods such as powder metallurgy and mechanical alloying [8,9], spark plasma sintering [10], laser cladding [11] and electrodeposition are used. Mechanical alloying offers an opportunity to prepare alloys

* Corresponding author. Tel.: +48 60 228 9705; fax: +48 22 822 4889.
E-mail address: stojek@chem.uw.edu.pl (Z. Stojek).
[1] ISE member.

0013-4686/$ – see front matter © 2004 Elsevier Ltd. All rights reserved.
doi:10.1016/j.electacta.2004.08.028

of various structural and chemical factors that are important for their final catalytic properties [8]. The electrodeposition approach to the production of the Ni–W alloys has also some apparent advantages, i.e. nanocrystalline/amorphous materials can be obtained and there is a possibility to control the grain size of the alloys from several to hundreds of nanometers. In addition, thin layers of the alloys can be plated on a surface of any shape and there is no post-processing requirement.

For the electrodeposition of the amorphous molybdenum alloys with the iron-group metals the citrate–ammonia baths are used in most of the cases [12–16]. However, if the content of Mo does not exceed 12–13 at.%, the deposits obtained in the citrate ammonia bath consist of just one crystallographic phase, i.e. the solid solution of Mo in nickel [13,14]. Then the structure of the alloy is polycrystalline. When the content of Mo increases up to 18 at.%, the initial indications of the formation of the amorphous/nanostructured phase arise. The alloys become really amorphous/nanostructured when the content of Mo exceeds 22–25 at.%. The electrodeposition of such a high-molybdenum-content alloys from the citrate–ammonia solution is possible, however, the very-high-molybdenum-content alloys (63 or 38 at.% of Mo), independently of the alloy deposition rate, exhibit cracks and small pits which diminishes their practical importance [15].

The nickel alloys can be also deposited from other baths. The pyrophosphate bath has been employed for the electrodeposition of nickel [17], and nickel alloys with Cu [18], Fe [19] and Sn [20]. A possibility of electrodeposition of the Ni–Mo alloys from pyrophosphate bath was mentioned some time ago by Stasov and Pasechnik [21] and recently by Jovic et al. [22]. The composition proposed in Ref. [21] enables the deposition of the alloys under reasonable current efficiency at room temperature with Mo content up to 40 wt.%. The deposits are well adhered to the copper and steel substrates. Also, the content of Mo in the alloys does not depend substantially on temperature in the range 20–40 °C. The Ni–Mo alloys electrodeposited by pulse current [22] might contain up to 41 at.% of Mo. A current-efficiency drop below 10% accompanied that high content. Moreover, the morphology of the deposits was particularly sensitive to the co-evolution of hydrogen, and most of the deposits exhibited a dense net of bumps and cracks.

The aim of this work was to modify the pyrophosphate bath so that thin layers of Ni–Mo alloys of good appearance, integrity and smoothness could be obtained. Such smooth layers are advantageous from e.g. trybological point of view. The above aim has been achieved by adding 2-butyne-1,4-diol and rokafenol N-10 (polyoxyethylene–phenol class nonionic detergent) to the bath, which compounds were used successfully in the electrodeposition of tungsten alloys [23–25]. The pyrophosphate bath should be more resistive to degradation (oxidation) compared to citrates. The influence of various factors on the current efficiency, the deposition rate, the molybdenum content and the structure of the alloys have been examined.

2. Experimental procedure

All of the alloys where deposited using an EG&G PARC galvanostat/potentiostat model 173A. The electrodepositions were done in a special plating cell, with two symmetrically placed anodic compartments, separated from the cathodic chamber with glass frits. Two inert, passivated titanium electrodes (TiO_2/RuO_2) were used as the anodes. The area of each anode was circa 10 cm^2. Polished Cu–Zn brass and steel plates and silicon wafers with vapour deposited Cu (Kocour, Chicago, and Plating Test Cell Supply Company, Cleveland, OH) had the working area of 2 cm^2 and were used as the substrates for the deposits. However, all the results shown in the figures, except for Fig. 5, were obtained with brass substrates. Just before plating the substrate was degreased and slightly etched and activated with dilute sulfuric acid.

Polarization experiments were done with the three-electrode system using a type PI-50-1.1 potentiostat/galvanostat, Russia, connected with a PR-8 function generator. A platinum sheet served as the counter electrode and a SCE was the reference electrode. The top of a copper rod of the working area equal to 0.125 cm^2 was used as the working electrode. Before each experiment the surface of the electrode was coated with either Ni or Ni–Mo in the examined solution for 30 min. The ohmic drop was evaluated in separate experiments by switching the galvanostatic pulse off after 30 s of electrolysis and measuring the resulting potential drop with the use of an oscilloscope.

The solution with the main components at the concentrations such as those reported for the electrodeposition of molybdenum alloys by Stasov and Pasechnik [21] was the starting point in this work. Stasov's solution is called the *initial solution* throughout this paper and its composition can be written as: $Na_4P_2O_7{\cdot}10H_2O$—160 g dm^{-3}, NH_4Cl—20 g dm^{-3}, $NiSO_4{\cdot}7H_2O$—40g dm^{-3} and $Na_2MoO_4{\cdot}2H_2O$. The suggested pH value for the *initial solution* is 8.5. pH of the final solutions was adjusted by adding appropriate amounts of 30% ammonium solution. In the course of the work the *initial solution* was changed by adding 2-butyne-1,4-diol—50 mg dm^{-3} and rokafenol N-10 (nonionic detergent)—100 μl dm^{-3}, and by varying the concentration of Na_2MoO_4 in the bath. All solutions were prepared using deionized water produced by a NanoPure Milli-Q purification system, Millipore. The alloys were deposited at 20 °C.

Compositions of the deposits were examined using a Roentec, model M1, EDX analyzer (Germany) integrated with a LEO, model 435 VP, scanning electron microscope (SEM). The mean from the multiple EDX composition data, the weight of the alloy layer and the assumption that six and two electrons are used in the reduction of the Mo and Ni ions, respectively, allowed the calculation of the current efficiency. The deposition rates have been calculated from the difference in the weight of the substrates after and before deposition.

A NanoScope scanning tunneling microscope (STM) was used to observe the alloy surfaces and to estimate their

smoothness. In the STM study, the tunneling current was set in the range up to 1 nA and the bias voltage up to 300 mV. The scanning rate was varied from 0.9 to 2.0 Hz. The STM data obtained were further computer processed to create 3D images and to perform a roughness analysis.

The structure of the deposits was determined by the X-ray diffraction method using a DRON-1 instrument equipped with a Fe X-ray tube (Kα: λ = 1.9373 Å).

3. Results and discussions

3.1. Influence of electrodeposition conditions on composition and deposition rates of Ni–Mo alloys

The Ni–Mo alloys electrodeposited from the bath corresponding to the *initial solution* are rather rough due to the presence of many micro-sphere fragments on the surface. The introduction of the brightening and wetting agents into the baths makes the surface much smoother and eliminates the cracks in the alloy layer. The bumps and spheres virtually disappear from the surface. This is illustrated in Fig. 1A and B. The edges of the covered support plates (not shown in Fig. 1) are also reasonably smooth and well defined. The additives used together lower the surface tension, adsorb on the alloy surface, decrease the hydrogen evolution at a given Mo content, keep the seed size small and apparently help to keep the deposition rate at similar level throughout the surface.

The dependencies of the molybdenum content and the deposition rate versus Na_2MoO_4 concentration for the solutions with and without 2-butyne-1,4-diol and rokafenol are shown in Fig. 2. Apparently, the amount of Mo in the alloys increases up to 33–35 at.% with increasing the concentration of the molybdate ion in the bath. This increase is accompanied by a decrease in the deposition rate. The decrease in the deposition rate (expressed in mg h^{-1} cm^{-2}) is a result of the decrease in the current efficiency from 50–57% to 2–10% (pH 8.5; j = 30 mA cm^{-2}). The primary cause of these changes is an enhancement in the catalytic properties of nickel towards the evolution of hydrogen, which takes place after adding molybdenum to nickel. Furthermore, for a fixed concentration of the molybdate ions in the solution, the content of Mo in the alloys is smaller by up to 7% when the deposition is carried out in the presence of the brightening and wetting agents.

The deposition rate is very low at low current densities applied while the Mo content in the formed Ni–Mo alloy exceeds 30 at.%. This is illustrated in Fig. 3. In this case, i.e. at the potentials corresponding to low current densities, molybdenum is deposited preferentially [21]. Since the exchange current density for the hydrogen evolution for Ni–Mo alloys in the alkaline solutions is relatively high and can reach the values up to 11 mA cm^{-2} [26], the hydrogen evolution becomes the major electrode process. Therefore, the alloy deposition rate decreases. With an increase in current density, the cathode potential becomes more negative, the

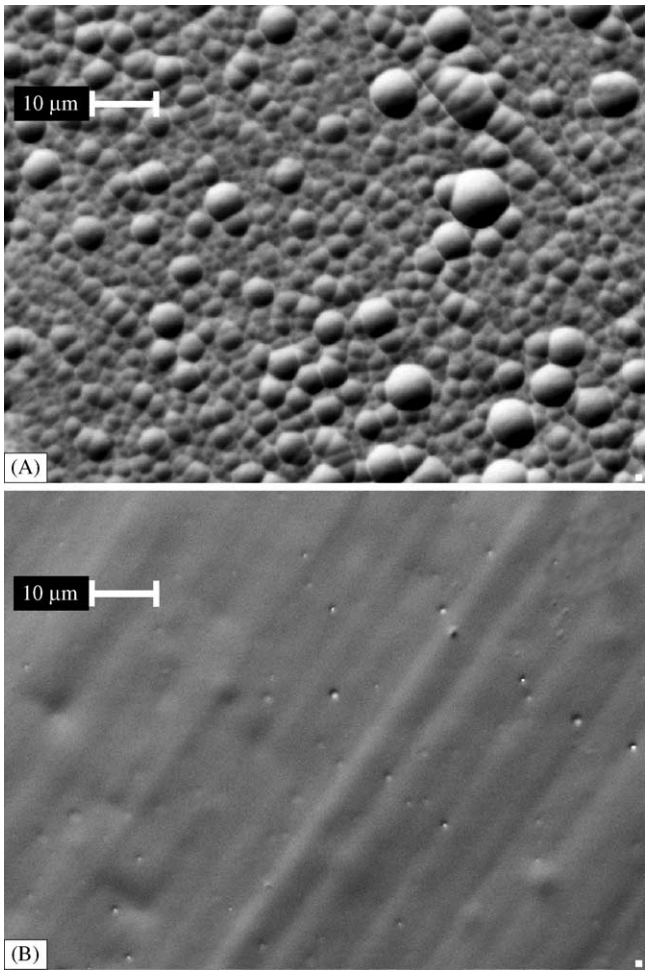

Fig. 1. SEM images of Ni–Mo alloy (84:16 at.%) deposits on iron covered with Zn–Cu brass layers obtained with j = 30 mA cm^{-2} from solutions. (A) *Initial solution* with 4 g dm^{-3} of $Na_2MoO_4{\cdot}2H_2O$, as proposed in [21]. (B) *Initial solution* (as is A) containing also 2-butyne-1,4-diol (50 mg dm^{-3}) and rokafenol (100 μl dm^{-3}).

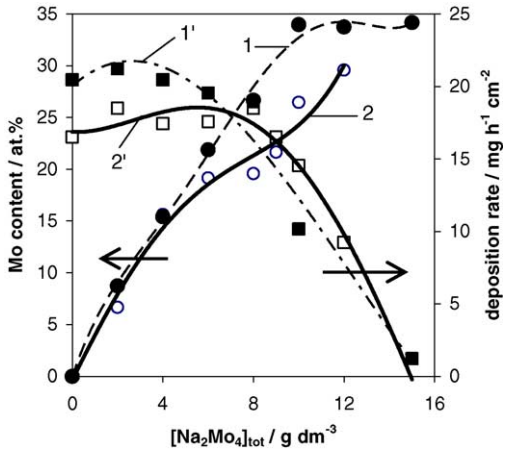

Fig. 2. Influence of Na_2MoO_4 concentration in the bath on Mo content in Ni–Mo alloys (1, 2; left axis) and on deposition rate of alloys (1′, 2′; right axis). Baths composition: 1′, 2′—that of *initial solution*; 1, 2—*initial solution* with 2-butyne-1,4-diol (50 mg dm^{-3}) and rokafenol (100 μl dm^{-3}). Current density: 30 mA cm^{-2}. The arrows indicate corresponding ordinate axis.

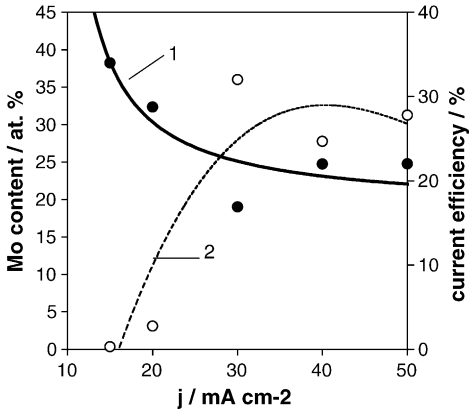

Fig. 3. Effect of current density on Mo content in Ni–Mo alloys (1, left axis, filled circles) and on current efficiency (2, right axis, open circles). Bath composition: *initial solution* containing also 6 g dm^{-3} of $Na_2MoO_4{\cdot}2H_2O$, 2-butyne-1,4-diol (50 mg dm^{-3}) and rokafenol (100 μl dm^{-3}).

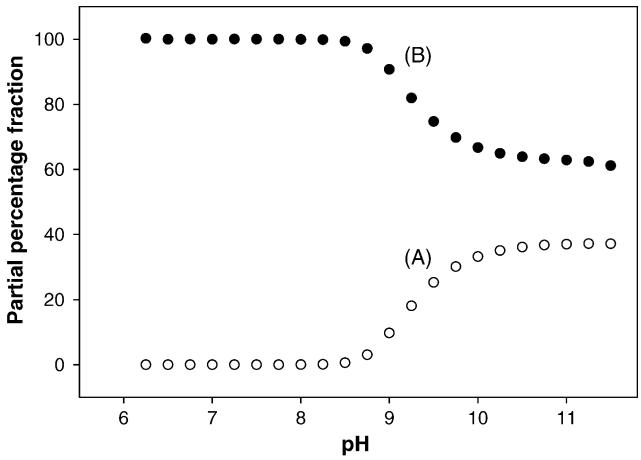

Fig. 4. Calculated percentage fractions of all ammonia (A) and pyrophosphate (B) nickel complexes in total Ni(II) plotted as functions of pH. Solution composition: 0.36 M $Na_4P_2O_7$ + 0.14 M $NiSO_4$ + 0.374 M NH_4Cl.

electroreduction of Ni(II) accelerates and the contents of molybdenum in the alloys decreases. This causes an increase in the overvoltage for the hydrogen evolution and correspondingly an increase in the deposition rate.

pH influences the Mo content in the alloys and the deposition rate. Some examples are presented in Table 1. As it follows from these data, the content of Mo increases with decreasing pH in the range 8.5–10, while the deposition rate and the current efficiency decrease. The increase of pH above 10 neither affects substantially the deposition rate nor the current efficiency.

The relation between the contents of Mo and pH is strikingly similar to the dependence of the partial percentage fractions of Ni pyrophosphate species and the Ni–ammonia complexes on pH. These percentage fractions have been calculated using the available formation constants for all pyrophosphate and ammonia complexes, and are plotted versus pH in Fig. 4. In the pH range from 8.5 to 10 a substantial drop in the fraction of the Ni–pyrophosphate complexes and an increase in the fraction of the Ni–ammonia complexes take place. The absolutely dominating species in the bath is $NiP_2O_7^{2-}$ and, within the ammonia complexes, $Ni(NH_3)_4^{2+}$ and $Ni(NH_3)_3^{2+}$. It is very probable that by analogy to the deposition of Ni–W alloys in the citrate bath [27,28], for which the importance of a bimetallic complex $[(Ni(WO_4)Cit)(H)]^{2-}$ in the deposition process has been shown, in the pyrophospate bath, a bimetallic complex of Ni, molybdate and pyrophosphate is the key intermediate species. For the deposition of the Ni–Mo alloys in the citrate bath it has also been suggested that the electroreduction of MoO_4^{2-} to Mo proceeds in several steps, one of which is the formation of an intermediate species, probably MoO_2 [29,30] or $(NiCitMoO_2H_3)_{ads}^{-}$ [15].

The pH effect on the deposition rate and the Mo content in the alloys is not easy to explain either. This is just because the electrodeposition is accomplished by several conjugated and pH-dependent reactions. After taking into account the formation of various Ni(II) complexes in the pyrophosphate baths, the Nernst potentials for both Ni and Mo couples can be estimated as circa −0.6 V. So, as it can be seen from the polarization curves presented in Fig. 5, the electrodeposition of both Ni and Ni–Mo alloy occurs under kinetic control (with some overpotential). A similar effect was also observed during the

Table 1
Mo contents, deposition rate and current efficiency for Ni–Mo alloys deposited at various pH from *initial solution* containing additionally 12 g dm^{-3} of $Na_2MoO_4{\cdot}2H_2O$, 2-butyne-1,4-diol (50 mg dm^{-3}) and rokafenol (100 μl dm^{-3}), j = 30 mA cm^{-2}

pH	Contents of Mo (at.%)	Deposition rate (mg h^{-1} cm^{-2})	Current efficiency (%)
8.5	29.7	9.1	16.5
9.0	22.1	15.6	32.7
9.75	19.7	14.4	31.5

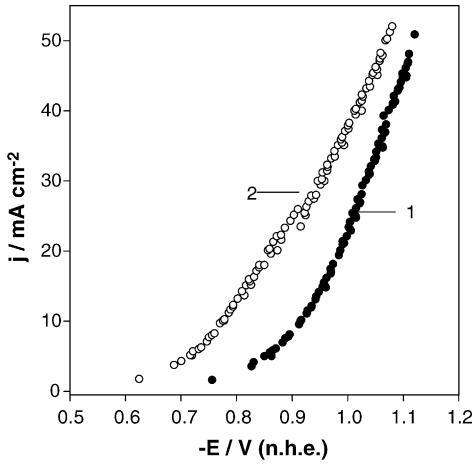

Fig. 5. Galvanostatic polarization curves for Ni (1) and Ni–Mo alloy on copper (2) electrodes in the *initial solution* containing also 2-butyne-1,4-diol (50 mg dm^{-3}), rokafenol (100 μl dm^{-3}), and $Na_2MoO_4{\cdot}2H_2O$ at concentration 0 g dm^{-3} (1) and 10 g dm^{-3} (2) (pH 8.5).

Table 2
Mo content at various distances from the substrate

Distance from substrate	Mo content (at.%)	
	Sample 1	Sample 2
15–25 μm, top of layer	12.9 ± 0.5	23.3 ± 1.1
1 μm	13.2 ± 0.5	–
Close to substrate	10.7 ± 0.7	24.0 ± 0.7

Alloy deposited at current density of 30 mA cm^{-2} from *initial solution* containing 2-butyne-1,4-diol (50 mg dm^{-3}), rokafenol (100 μl dm^{-3}) and $Na_2MoO_4{\cdot}2H_2O$ at concentration 4 g dm^{-3} (sample 1, pH 9.23) and 9 g dm^{-3} (sample 2, pH 8.75).

Ni–Mo electrodeposition from the citrate–ammonium baths [13]. Apparently, the hydrogen evolution process is faster at the Ni–Mo alloy compared to that at the Ni electrode. An increase in pH results in decreasing the current related to the hydrogen evolution and, correspondingly, in increasing the alloy deposition rate.

The Mo content in the alloy was determined at several points on the surface of the fracture cross-section. Three locations are selected for Table 2: (a) the position as close as possible to the copper substrate; (b) that at the distance of circa 1 μm from the substrate; (c) on the top of the deposit. As it follows from the data presented in Table 2, the content of Mo in the alloys is almost uniform and independent of the film thickness. A small decrease (not shown in the table) in the Mo content from 23.3 to 21.8 at.% is obtained at the substrate edges (the thickness of the films examined was circa 40 μm). This decrease is rather caused by the increase in the current density at the edges (diffusional edge effect).

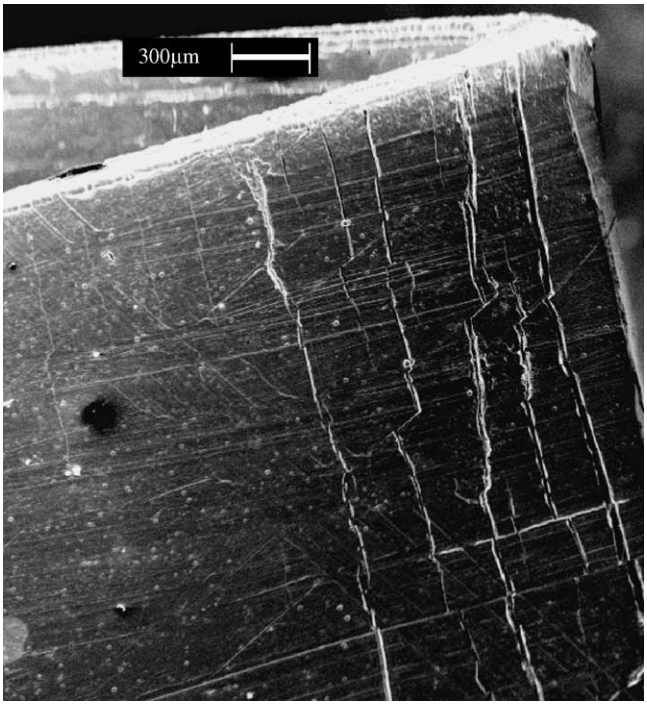

Fig. 6. SEM micrograph of a folded sheet coated by Ni–Mo alloy (13 at.% of Mo). Thickness of deposit: circa 15 μm. Current density: 30 mA cm^{-2}.

The deposited Ni–Mo alloys adhere well to copper-, brass- and iron substrates. The deposits can be folded without evident peeling. Only some cracks may appear in the folding area. This is illustrated in Fig. 6.

3.2. X-ray diffraction and SEM analysis

A brief analysis of the X-ray diffractograms of the electrodeposits obtained from the plating pyrophosphate bath leads to a conclusion that an addition of molybdenum to the deposit changes its texture. The atom arrangement changes from (2 2 0) preferred for pure-nickel deposits to (1 1 1) for the alloys containing 15 and more at.% of Mo. Fig. 7 presents selected diffraction spectra obtained for the deposits plated from the pyrophosphate bath. The structure of the electrodeposited Ni–Mo alloy becomes amorphous-like (the appropriate widening of the diffraction peaks appears) when the amount of molybdenum exceeds 20 at.%. Characteristic changes in the patterns of the fracture cross-sections obtained for various deposits are shown in Fig. 8. Apparently, the structure of the deposits transforms from that typically columnar

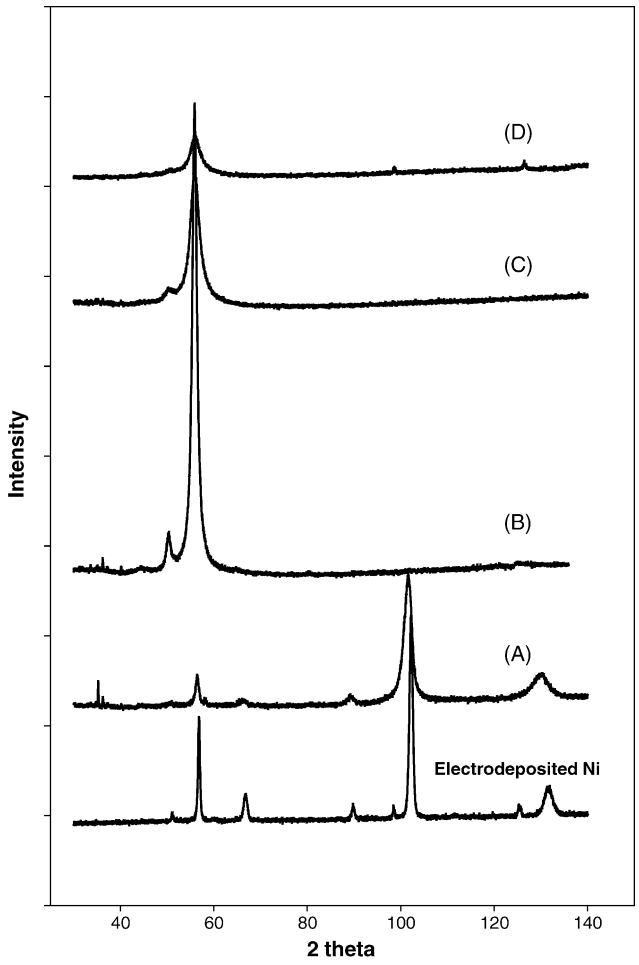

Fig. 7. X-ray diffractograms obtained for Ni and Ni–Mo alloys plated from pyrophosphate baths. Mo content: 6.9 at.% (A), 15.6 at.% (B), 21.7 at.% (C) and 23.9 at.% (D). Current density: 30 mA cm^{-2}.

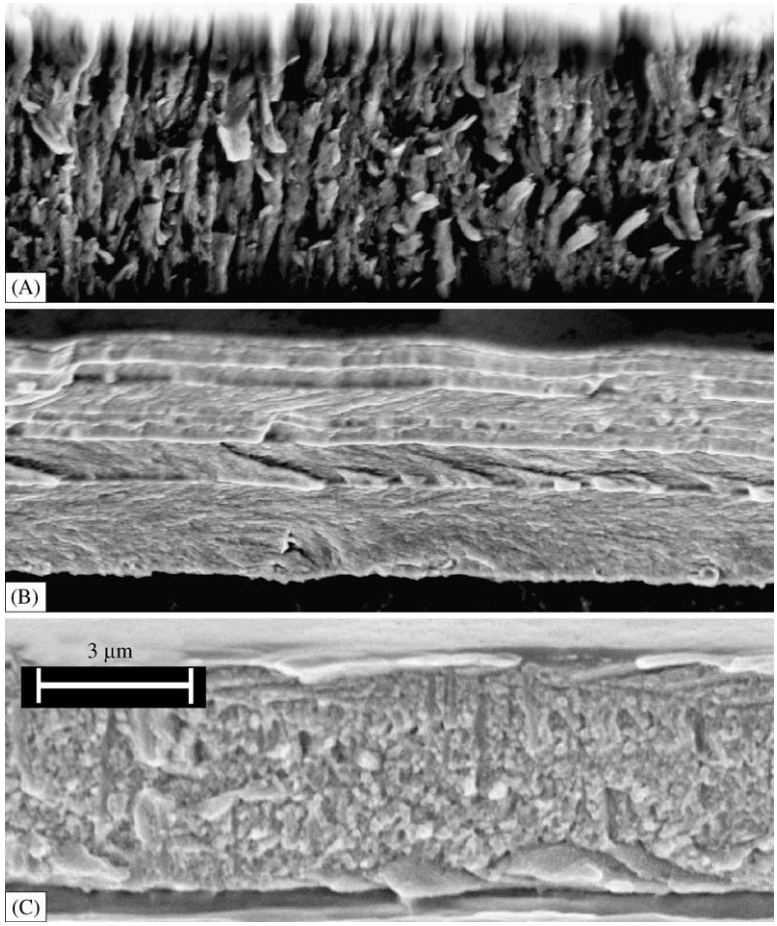

Fig. 8. SEM images of fracture cross-sections of thin (several μm) layers of Ni and various Ni–Mo alloys deposited from pyrophosphate bath. Current density: 30 mA cm^{-2}: (A) Ni; (B) Ni–Mo alloy with 6.23 at.% of Mo; (C) Ni–Mo alloy with 23.89 at.% of Mo.

observed for pure Ni to a uniform-like for the deposits with a high Mo content. The most pronounced irregularities in the fracture cross-section structure, seen as multilayer fracture, start at the Mo content of 6–8 at.%. This is probably related to the beginning of the transformation of the deposit texture from (2 0 0) to (1 1 1). The deposits with Mo content higher than 15 at.% have an almost uniform appearance of their fracture cross-sections. However, it is possible to observe slight irregularities in their structure along the direction perpendicular to the substrate. Namely, the first circa 5 μm of the alloy layer (those located next to the substrate) give cracks slightly irregular, while the rest of the layer brakes very uniformly. This difference in the morphology of the deposit can be caused by the changes in the orientation of the nanocrystals in the internal and the external layers or by the transformation of the deposits from nanocrystalline to glass-alike structure. Interestingly, the above differences in the morphology of the cross-brakes do not result in significant changes in the X-ray diffraction patterns.

The diffractograms obtained for both 7 and 30 μm thick deposits exhibit the shapes typical for the nanostructured deposits and contain one broad peak placed in the same 2θ position. The mean crystal sizes determined from the peak width using the Scherrer equation modified by Warren and Biscoe are 93 and 113 Å for the 7 and 30 μm deposits, respectively. It suggests that the changes in the fracture cross-section patterns seen in Fig. 8 are caused by the reasons independent of the nanocrystal size.

Some changes in the crystal grain size can be observed for the deposits with various Mo content: the lower the molybdenum content the larger are the crystals. The calculated grain sizes for the alloys of various Mo content are shown in Table 3. It is clear that with increase in molybdenum content the Ni–Mo alloy changes its structure from micro- to nanocrystalline. The change in the 2θ value for the signal placed in the position corresponding to the Ni (1 1 1) plane ($2\theta = 56.88^\circ$, referred to Fe Kα) gives additional information regarding the deposited alloys. The changes in the d(1 1 1) distance plotted versus molybdenum content in the alloy are shown in Fig. 9. This distance increases linearly in the range of Mo content up to 15 at.%. Such a phenomenon is typical for the formation of solid solution of two mixed metals. At the Mo content of 16–20 at.% d reaches a maximum and then starts to decrease. This may be related to the formation of

Table 3
Estimated grain size and $d(1\,1\,1)$ distance obtained for Ni and Ni–Mo deposits plated from the pyrophosphate bath

Mo content (at.%)	Estimated grain size (Å)	(1 1 1) maximal intensity 2θ	$d(1\,1\,1)$ (Å)
0	415	56.84	2.0353
6.9	313	56.44	2.0485
8.5	280	56.24	2.0552
15.6	304	55.88	2.0673
19	168	55.92	2.0660
21.4	113	56.04	2.0619
21.7	94	56.04	2.0619
23.9	77	55.90	2.0667
24.8	61	56.20	2.0565

either nanocrystals of pure Mo that cannot be dissolved in Ni or of disturbed structure of known intermetallic Ni_4Mo compound. Another evidence for the transformation phenomenon is the parallel decrease in the estimated crystal size observed in the same region of Mo content.

When the Mo content exceeds 20 at.% the alloy looks smoother in its fracture cross-section images and gives wide X-ray diffractograms, which proves that the deposit is more uniform, probably nanostructured. The results obtained in this work agree well with the theoretical calculations done by Zhang et al. [31], who have determined, by using the molecular dynamics simulation, that the glass forming range of the Ni–Mo binary system starts at 21 at.% of Mo in Ni.

As we have found, similarly to the increase in the molybdenum content, the codeposition of phosphorus (reduction of hypophosphates) with nickel and molybdenum results in a nanostructured material. For example, an addition of 8 at.% of phosphorus to the Ni–Mo alloy of 6:1 ratio decreases the grain size from 300 to 45 Å. The addition of phosphorus leads also to significant smoothing of the fracture cross-section structure of the layers.

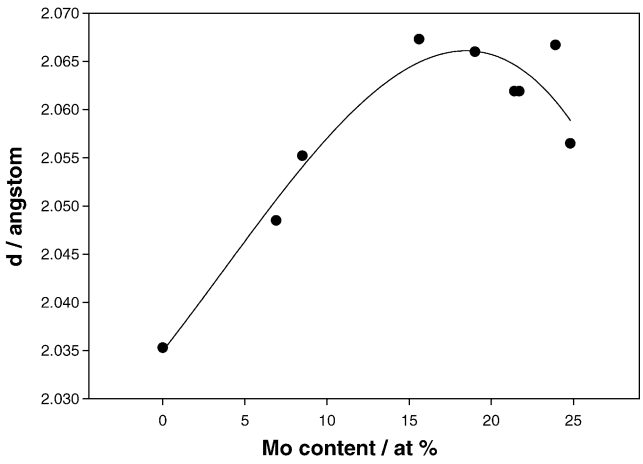

Fig. 9. Changes in mean $d(1\,1\,1)$ distance in Ni–Mo alloy deposits containing increasing amount of Mo in nickel. Points are experimental, line is a polynomial cubic function fitted to the points.

3.3. STM examination

The surface roughness of the Ni–Mo alloys was examined by STM. The growing Ni–Mo alloy forms a fine structure already at the early stages. When the thickness of the film increases, the surface becomes more uniform and smoother, and the characteristic pattern of the substrate is eliminated. This can be seen in Fig. 10A and B. When the Mo content in the alloys does not exceed 25–30 at.% and the thickness of the film is in the range from 0.25 to 12 μm, the smallest roughness of electrodeposited Ni–Mo alloys is 1–3 nm (on a 5 μm × 5 μm area scanned). The thin, perpendicular to the surface, crystallites have the thickness of circa 10–50 nm, however, their length is limited. This conclusion can be drawn after comparing the STM image in Fig. 10B with the SEM micrograph of the fracture cross section given in Fig. 8C. Apparently, the long, nanometer thick needles seen in the amorphous/nanocrystalline Ni–W alloys [32] are not formed in the Ni–Mo alloy.

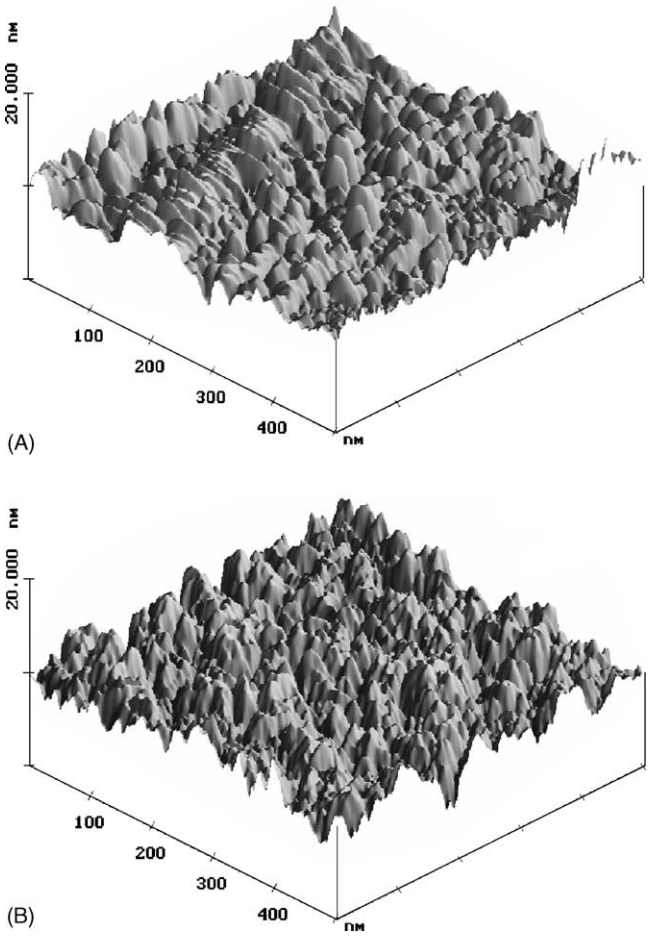

Fig. 10. STM surface images of: brass substrate (A), and Ni–Mo alloy (16 at.% Mo) electrodeposited from *initial solution* containing 4 g dm^{-3} of $Na_2MoO_4{\cdot}2H_2O$, 1,4-butyndiol (50 mg dm^{-3}) and rokafenol (100 μl dm^{-3}) at current density of 30 mA cm^{-2} (B). Thickness of coating: circa 12 μm.

4. Conclusions

Similarly to the deposition of Ni–W alloys from the citrate bath, the addition of wetting agents such as 2-butyne-1,4-diol and rokafenol N-10 to the pyrophosphate bath resulted in the removal of bumps, spheres and cracks from the Ni–Mo alloy surface.

On the other hand, there is no similarity between the fibrous, nanocrystalline structure of the Ni–W alloys, where the needles grow perpendicular to the support surface, and the structure of the Ni–Mo amorphous alloys. For the Ni–Mo system, the nanocrystallites are rather oval. The amorphous/nanocrystalline structure appears for the deposits of Mo content higher than circa 20 at.%. In addition, at that content of Mo, the transformation of the solid solution of Mo in Ni into either the deformed structure of Ni_4Mo or a mixture of the saturated Ni–Mo solid solution with nanostructured Ni takes place.

Acknowledgement

HC thanks the Polish Foundation Kasa Mianowskiego for a fellowship.

References

[1] D. Landolt, Plating Surf. Finish. 88 (2001) 70.
[2] T.E. Tsenta, V.M. Knyazheva, T.V. Svistunova, Y.M. Kolotyrkin, D.S. Zakharin, Prot. Met. 25 (1989) 28.
[3] C.-C. Hu, C.-Y. Weng, J. Appl. Electrochem. 30 (2000) 499.
[4] W.K. Hu, X.J. Cao, F.P. Wang, Y.S. Zhang, Int. J. Hydrogen Energy 22 (1997) 621.
[5] C. Fan, D.L. Piron, A. Steb, P. Paradis, J. Electrochem. Soc. 141 (1994) 382.
[6] J.F. Kriz, H. Shimada, Y. Yoshimura, N. Matsubayashi, A. Nishijima, Fuel 74 (1995) 1852.
[7] M.P. Astier, G. Dji, S.J. Teichner, Appl. Catal. 72 (1991) 321.
[8] P. Kedzierzawski, D. Oleszak, M. Janik-Czachor, Mater. Sci. Eng. A 300 (2001) 105.
[9] D. Oleszak, V.K. Portnoy, H. Matyja, Mater. Sci. Forum 312 (4) (1999) 345.
[10] S.D. De la Torre, D. Oleszak, A. Kakitsuji, K. Miyamoto, H. Miyamoto, R. Martinezm-S, F. Almeraya-C, A. Martinez-V, D. Rios-J, Mater. Sci. Eng. A 276 (2000) 226.
[11] G.L. Goswami, S. Kumar, R. Galun, B.L. Mordike, Lasers Eng. 13 (2003) 1.
[12] L.S. Sanches, S.H. Domingues, C.E.B. Marino, L.H. Mascaro, Electrochem. Commun. 6 (2004) 543.
[13] L.I. Stepanova, O.G. Purovskaja, V.V. Sviridov, Russ. J. Appl. Chem. 73 (2000) 66.
[14] L.I. Stepanova, O.G. Purovskaja, V.N. Azarko, V.V. Sviridov, Proceedings of the Academy of Sciences of Belarus, Ser. Chem. Sci. (1997) 38 (in Russian).
[15] E.J. Podlaha, D. Landolt, J. Electrochem. Soc. 143 (1996) 885.
[16] E.J. Podlaha, D. Landolt, J. Electrochem. Soc. 143 (1996) 899.
[17] V.A. Purin, Metal electrodeposition from pyrophosphate baths, Riga (1975) 194 (in Russian).
[18] M. Ishikawa, H. Enomoto, M. Matsuoka, Ch. Iwakura, Electrochim. Acta 40 (1995) 1663.
[19] A. Ramachandran, C.N. Tharamani, S.M. Mayanna, Trans. Inst. Met. Finish. 79 (2001) 195.
[20] V.V. Orekhova, I.D. Roi, Sov. Electrochem. 27 (1991) 638.
[21] A.A. Stasov, S.A. Pasechnik, Izv. Vysh. Uch. Zav., Ser. Chem. and Chem. Technol. 16 (1973) 600 (in Russian).
[22] V.D. Jovic, B.M. Jovic, G.R. Stafford, AESF Proceedings, 2003.
[23] M. Donten, Z. Stojek, Polish J. Chem. 68 (1994) 1193.
[24] M. Donten, H. Cesiulis, Z. Stojek, Electrochim. Acta 45 (2000) 3389.
[25] H. Cesiulis, A. Baltutiene, M. Donten, M.L. Donten, Z. Stojek, J. Solid State Electrochem. 6 (2002) 237.
[26] S.D. De la Torre, D. Oleszak, F. Almeraya, A. Martinez, R. Martinez, D. Rios, H. Miyamoto, Mater. Sci. Forum 343 (3) (2000) 855.
[27] O. Younes-Metzler, L. Zhu, E. Gileadi, Electrochim. Acta 48 (2003) 2551.
[28] O. Younes-Metzler, E. Gileadi, J. Electrochem. Soc. 149 (2002) 100.
[29] S. Rengakuji, Y. Nakamura, M. Inoue, K. Nishibe, H. Imanaga, Denki Kagaku 59 (1991) 885.
[30] Y. Zeng, M. Ma, X.M. Xiao, Z.L. Li, S.X. Lian, S.M. Zhou, Chin. J. Chem. 18 (2000) 29.
[31] Q. Zhang, Z.C. Li, C. Lin, B.X. Liu, E. Ma, J. Appl. Phys. 87 (2000) 4147.
[32] M. Donten, Z. Stojek, H. Cesiulis, J. Electrochem. Soc. 150 (2003) 95.